

Bandwidth-Scalable Long-Haul Transmission Using Synchronized Colorless Transceivers and Efficient Wavelength-Selective Switches

Daniel J. F. Barros, Joseph M. Kahn, *Fellow, IEEE*, Jeffrey P. Wilde, *Member, IEEE, Member, OSA*, and Tarek Abou Zeid

Abstract—We propose a modular scalable long-haul architecture supporting variable-bandwidth channels with bit rates from 100 Gbit/s to beyond 1 Tbit/s. Colorless transceivers have two operating modes. One transceiver can transmit/receive a conventional narrow-band channel occupying a 30-GHz bandwidth and conveying 100 Gbit/s, or a set of M transceivers can cooperate to transmit/receive a wideband channel occupying an $M \times 50$ -GHz bandwidth and conveying roughly 160 Gbit/s per 50 GHz (assuming polarization-multiplexed quaternary phase-shift keying). A colorless wavelength-selective switch supports two modes of add/drop (or (de)multiplexing) operation. It can add/drop narrow-band channels (each from/to one port) with minimal loss, or can add/drop wideband channels (each from/to M ports) without spectral gaps, with an additional loss not exceeding 1/3 (-4.8 dB), independent of M . Transceivers can use either single-carrier modulation or orthogonal frequency-division multiplexing (OFDM). We analyze and simulate OFDM-based systems to determine key design requirements, especially for synchronization of cooperating transceivers. A representative design achieves 1520-km reach with 1.4-dB margin in a dispersion-managed network using only erbium-doped fiber amplifiers, improving average spectral efficiency from about 2 to nearly 3 bits/s/Hz.

Index Terms—Coherent detection, communication system performance, flexible bandwidth, long-haul systems, multicarrier optical systems, optical orthogonal frequency-division multiplexing (OFDM), ROADM, superchannels, terabit channels, variable bandwidth channels, variable rate, wavelength-selective switch (WSS).

I. INTRODUCTION

CURRENT long-haul systems using 50-GHz channel spacing transmit 100 Gbit/s per channel using polarization-multiplexed quaternary phase-shift keying (PM-QPSK), achieving a spectral efficiency of 2 bits/s/Hz. Because of spectral gaps caused by (de)multiplexers and wavelength-selective switches (WSSs), most current systems use symbol rates of about 29–32 GHz, wasting about a third of the available bandwidth. As Internet traffic grows, demand is emerging for channels carrying higher bit rates, such as 400 Gbit/s and

1 Tbit/s. Higher order modulation can increase spectral efficiencies and bit rates without increasing symbol rates. Because of higher signal-to-noise ratio (SNR) requirements and limits imposed by fiber nonlinearity, however, long-haul spectral efficiencies and bit rates can be doubled (using PM-16-QAM), but probably not quadrupled without decreasing reach substantially (this would require using PM-64-QAM). Increasing the symbol rate and channel spacing can increase the per-channel bit rate (and slightly increase the spectral efficiency), but this approach is limited by the bandwidths of optoelectronic and electronic transceiver components.

These issues have motivated research on “superchannels,” which are collections of constituent channels that are individually modulated and detected, and are wavelength-division multiplexed (WDM) with little or no guard band. This approach enables channels far wider than those that can be processed by individual transceivers, increasing both spectral efficiencies and per-channel bit rates. Superchannels have been demonstrated using either single-carrier (SC) modulation or coherent optical orthogonal frequency-division multiplexing (CO-OFDM).

Two different superchannel approaches are based on SC modulation. In Nyquist WDM [1], [2], constituent channels are spectrally shaped by optical filtering so they occupy a bandwidth close to the symbol rate, in order to minimize intersymbol interference (ISI) and intercarrier interference (ICI). Nyquist WDM requires frequency-locked optical carriers and tight filtering at the receiver in order to reduce ICI. The received signals are sampled at a rate of two samples per symbol and digital equalization is used to compensate for ISI caused by dispersion. In no-guard-interval coherent optical OFDM (NGI-CO-OFDM), also called all-optical OFDM [3]–[8], the symbol rates and spacing of constituent channels are precisely matched, and constituent channels have precise symbol and carrier phase synchronization, so they are mutually orthogonal in the absence of dispersion. Received signals are sampled at a rate at least four times the constituent channel symbol rate, and digital equalization is used to compensate for ISI and ICI caused by dispersion. In previous NGI-CO-OFDM work, a recirculating frequency shifter (RFS) has been used to generate a comb of phase-locked carriers, which are separated by a fixed demultiplexer and modulated to form constituent channels. This approach is efficient for transmitting a superchannel of fixed bandwidth at a fixed center wavelength, but limits tunability and flexibility.

Alternatively, superchannels can be formed from constituent channels modulated by CO-OFDM [9]–[11], which are detected and generated in the digital domain using the discrete

Manuscript received November 13, 2011; revised March 17, 2012, May 20, 2012; accepted May 24, 2012. Date of publication June 15, 2012; date of current version July 25, 2012. This work was supported by a Google Research Award.

The authors are with the E. L. Ginzon Laboratory, Department of Electrical Engineering, Stanford University, Stanford, CA 94305 USA (e-mail: djbarros@stanford.edu; jmk@ee.stanford.edu; jpwilde@stanford.edu; abouzeidtarek@hotmail.com).

Digital Object Identifier 10.1109/JLT.2012.2203585

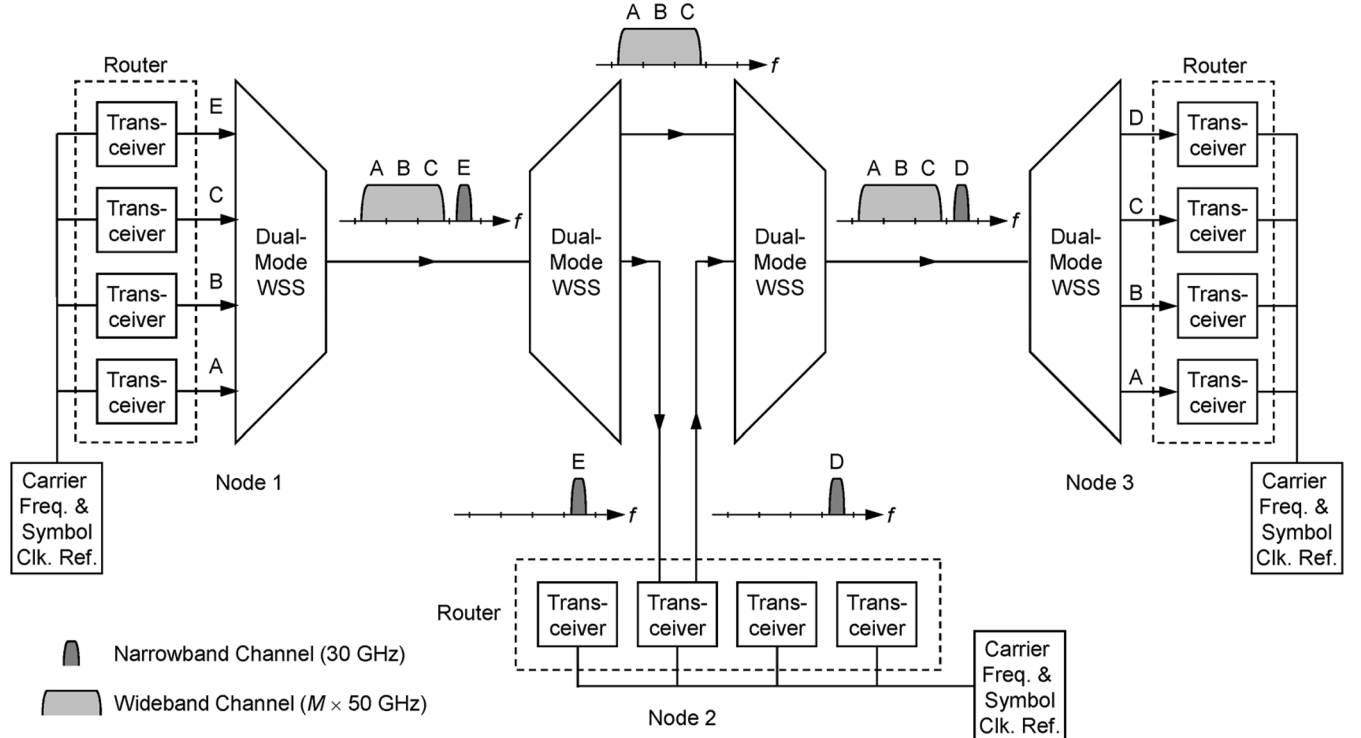


Fig. 1. Optical network with variable-bandwidth channels. Only west-to-east traffic is shown for simplicity.

Fourier transform and its inverse. The spacing between constituent OFDM channels is precisely equal to a multiple of the subcarrier spacing and, with a sufficiently long cyclic prefix, ISI and ICI can be avoided, even in the presence of dispersion. Previous studies generated CO-OFDM superchannels using a bank of lasers (or an RFS) with a single modulator, but did not fully address the symbol and carrier synchronization required for practical data transmission, particularly in a tunable flexible architecture.

In this paper, we propose a system architecture allowing superchannel bit rates to scale with traffic demands from 100 Gbit/s to over 1 Tbit/s (assuming PM-QPSK). Transceivers are colorless and operate at symbol rates not higher than 50 GHz, with sampling rates only slightly higher than the symbol rate. In one operating mode, each transceiver can transmit/receive a channel about 30 GHz wide, conveying 100 Gbit/s, at any wavelength. In another operating mode, M transceivers can cooperate to transmit/receive a superchannel occupying any M contiguous 50-GHz slots, conveying roughly 160 Gbit/s per 50 GHz. Cooperative transceiver operation avoids the need for dedicated superchannel transceivers that can process the full superchannel bit rate, which might be significantly underutilized, especially during early phases of network build-out. While the transceivers can use either SC modulation or CO-OFDM, in this paper, we study CO-OFDM in detail. The architecture includes the carrier frequency and clock references required to synchronize cooperating transceivers. A colorless WSS supports two modes of operation on each add/drop port. It can add/drop narrow-band channels (from/to one add/drop port) with minimal loss, or can add/drop wideband channels (from/to M add/drop ports) with an additional loss not exceeding 1/3 (-4.8 dB), independent of M .

This paper is organized as follows. In Section II, we describe the variable-bandwidth network architecture and the dual-mode WSS design. In Section III, we analyze the performance of dual-mode CO-OFDM transceivers in the presence of various impairments and establish synchronization requirements for the cooperative superchannel mode. We also present an exemplary system design, evaluating its performance in nonlinear fiber transmission. In Section IV, we consider a model network, comparing fixed- and variable-bandwidth architectures in terms of spectral efficiency and transceiver utilization. We present conclusions in Section V.

II. VARIABLE-BANDWIDTH NETWORK

A. Variable-Bandwidth Channels

Fig. 1 shows an example of the proposed network architecture using variable-bandwidth channels. Each node uses *colorless dual-mode transceivers*, each of which can modulate/demodulate signals over a bandwidth up to 50 GHz and is tunable to any wavelength within a band (e.g., the C band). A single transceiver can modulate/demodulate a *narrow-band channel*, occupying about 30 GHz within a 50-GHz slot, and conveying a bit rate of about 100 Gbit/s. Alternatively, a collection of M transceivers can cooperate to modulate/demodulate a *wideband channel*, which occupies M contiguous 50-GHz slots, where $2 \leq M \leq 8$. Allowing for guard bands of about 10 GHz at the lower and upper extremes, a wideband channel uses a bandwidth of about

$$B(M) = M \times 50 \text{ GHz} - 20 \text{ GHz} \quad (1)$$

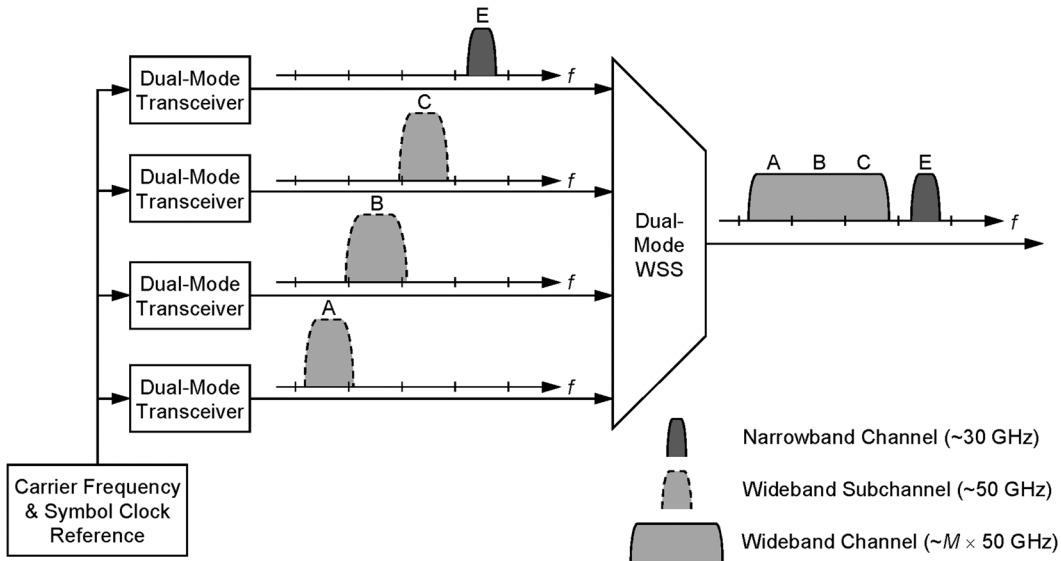


Fig. 2. Generation and multiplexing of narrow-band and wideband channels at node 1 of Fig. 1 using colorless dual-mode transceivers and a colorless dual-mode WSS.

and conveys a bit rate of roughly 160 Gbit/s per 50 GHz.¹ In Fig. 1, at a particular time instant at node 1, three transceivers cooperate to transmit wideband channel ABC, while a fourth transceiver transmits narrow-band channel E. At node 2, wideband channel ABC passes through, narrow-band channel E is dropped, and narrow-band channel D is added in its place. At node 3, wideband channel ABC and narrow-band channel D terminate.

Fig. 2 shows how channels are modulated and multiplexed at node 1 of Fig. 1. In particular, three transceivers modulate wideband subchannels A, B, and C. The lower and upper subchannels (A and C) have guard bands of about 10 GHz at the upper and lower extremes, while the interior subchannel (B) occupies nearly the full 50 GHz. A *colorless dual-mode WSS* multiplexes these subchannels without spectral gaps to form the wideband channel ABC. A detailed explanation of the dual-mode WSS is given in Section II-B.

In order for the subchannels comprising a wideband channel to be orthogonal, their carrier frequencies and symbol clocks must be synchronized. At each node, a carrier frequency reference comb and symbol clock reference are broadcast to all transceivers, and each transceiver locks its transmit laser to a comb frequency. The frequency comb is *not* demultiplexed into carriers to be modulated, which is a key to enabling colorless transceivers. Carrier and clock references at different nodes need not be mutually synchronized. Further details of the carrier and clock references and tolerable synchronization errors are given in Sections III-C and III-D.

Because of synchronization requirements and WSS constraints, all the subchannels comprising a wideband channel must originate at one node on contiguous WSS ports. Typically, these subchannels terminate together at another node.

¹WSS characteristics determine the required guard bands and thus the occupied bandwidths, which are adjusted by changing the number of used subcarriers in the CO-OFDM modulation. The bit rates assume PM-QPSK, and can be increased by using higher-order modulation. Precise guard bands, signal bandwidths and bit rates are given in Section III-E.

B. Colorless Dual-Mode WSS

The variable-bandwidth network shown in Fig. 1 requires a WSS that can add/drop each narrow-band channel from/to a single add/drop port and also add/drop M subchannels from/to M add/drop ports, without spectral gaps. Both functions can be performed using liquid crystal-on-silicon (LCOS) WSS designs [12]–[14]. The first function (analogous to an arrayed waveguide grating) could, in principle, be performed by an LCOS WSS without loss, although losses of about 5 dB are caused by diffraction and imperfect fiber-to-fiber coupling in typical devices [12]. The latter function (analogous to a star coupler) could be performed by setting the switching segments for the M subchannels to split light among M add/drop ports. This would lead to an additional loss of $1/M$ ($-10 \log_{10} M$ dB), which increases with M . Likewise, as M increases, this would require reducing the pixel pitch in the LCOS spatial light modulator (SLM).

In order to minimize the loss for WB channels, we propose a colorless LCOS WSS in which each add/drop port has two distinct operating modes. The *narrow-band mode* is used to add/drop one NB channel from/to a single add/drop port, and operates like a conventional LCOS WSS. The *wideband mode* is used to add/drop the M subchannels comprising an $M \times 50$ -GHz wideband channel from/to M add/drop ports, without spectral gaps. In the wideband mode, unlike a conventional LCOS WSS, the additional loss is $1/3$ (-4.8 dB), independent of M . In principle, when $M > 3$, the wideband loss of the dual-mode WSS may be lower than that of a conventional WSS used in combination with an ideal $1 \times M$ power splitter. The wideband mode requires all of the M subchannels to be added/dropped on physically contiguous add/drop fiber ports.

We note that the dual-mode WSS supports pass-through (expressing) of arbitrarily wide bands of spectrum, without gaps, just like a conventional LCOS WSS [12]–[14].

Wideband add and drop functions are performed in a reciprocal manner, so in order to explain the wideband mode most

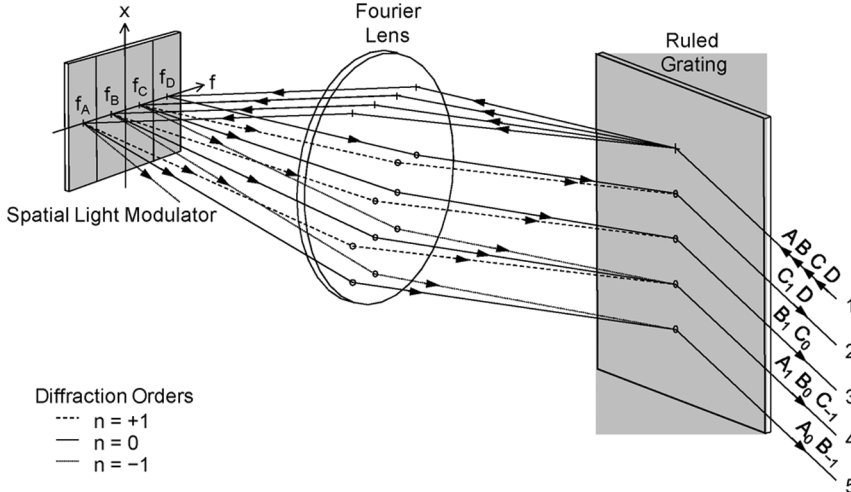


Fig. 3. Beam paths within the WSS at node 3 of Fig. 1. For simplicity, the express port is not shown, and only four drop ports are shown. On the SLM, f_A , f_B , f_C , and f_D denote the switching segments at the frequencies of (sub)channels A, B, C, and D, respectively. At drop ports 2, 3, 4, and 5, the subscripted labels denote the orders diffracted from the switching segments. For example, C_1 denotes the $+1$ order diffracted from switching segment f_C .

clearly, we will describe how the dual-mode WSS at node 3 in Fig. 1 demultiplexes wideband channel ABC into subchannels A, B, and C.

Fig. 3 shows beam paths within the WSS. Light from input port 1 is resolved by a ruled grating into its frequency components, which are incident upon an LCOS SLM. The SLM is subdivided into switching segments, whose width equals

$$w_{\text{seg}} = \frac{\partial\theta}{\partial f} f_{\text{lens}} \Delta v \quad (2)$$

where $\partial\theta/\partial f$ is the ruled grating angular dispersion, f_{lens} is the Fourier lens focal length, and Δv is the subchannel frequency spacing (here, 50 GHz). The SLM switching segments are labeled by the nominal center frequencies of the (sub)channels, f_A , f_B , f_C , and f_D . On switching segment f_D , a linear phase ramp steers narrow-band channel D to drop port 2. On switching segments f_A , f_B , and f_C , linear phase ramps steer wideband subchannels A, B, and C toward drop ports 3, 4, and 5. On these same switching segments, square-wave phase patterns are superposed on the linear ramps, splitting the beams equally into three diffraction orders, $n = -1, 0, +1$, causing each to fall onto three contiguous drop ports.

Fig. 4 shows schematically the phase patterns applied to these switching segments (switching segments f_A , f_B , and f_C employ different phase ramp slopes).

In order for the three diffraction orders to fall precisely onto three contiguous ports, the spacing between the ports d_{port} must be equal to

$$d_{\text{port}} = f_{\text{lens}} \alpha_{\text{sw}}. \quad (3)$$

Here, α_{sw} is the first-order diffraction angle from the square-wave phase pattern on the LCOS SLM, given by $\alpha_{\text{sw}} = \lambda/\Lambda$, where λ is the optical wavelength and Λ is the square-wave period. Presumably, condition (3) can be satisfied by existing LCOS WSS designs capable of splitting signals between multiple add/drop ports [12]–[14].

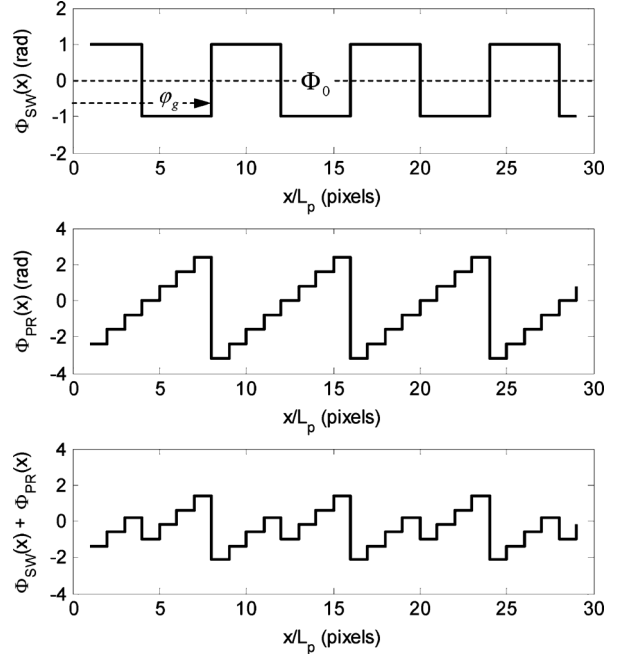


Fig. 4. Phase patterns applied to LCOS SLM switching segments to split and steer subchannels of a wideband channel. “SW” and “PR” denote “square wave” and “phase ramp,” respectively.

WSS simulation has been performed using a commercially available physical optics software package (DIFFRACT [15]). The LCOS SLM is modeled by an externally generated reflective phase mask that is imported into DIFFRACT.

Fig. 5 shows the intensity transfer functions from input port 1 to drop ports 2, 3, 4, and 5.

At port 2, intended for narrow-band channel D, the transfer function $H_{12}(f)$ includes the desired passband for channel D, which is steered to port 2 by switching segment f_D . This passband exhibits significant rolloff at the nominal band edges at $f - f_B = 75$ and 125 GHz, because portions of the beam diffracted from the ruled grating are incident on neighboring

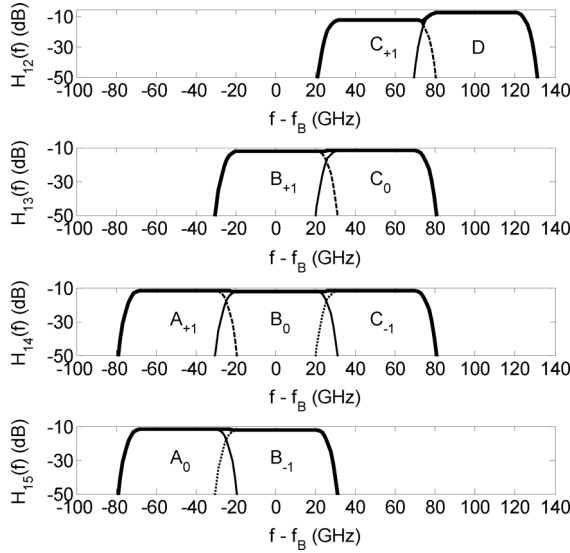


Fig. 5. Intensity transfer functions from input port 1 to drop ports 2, 3, 4, and 5 for the WSS at node 3 of Fig. 1, with beam paths described in Fig. 3. Diffraction orders $n = -1, 0$ and $+1$ are represented as dotted, solid and dashed lines, respectively. Subscripted labels denote the orders diffracted from the switching segments. For example, C_1 denotes the $+1$ order diffracted from switching segment f_C .

switching segments. That passband (labeled D) has an insertion loss of -7.0 dB caused by grating diffraction loss² and imperfect fiber-to-fiber coupling within the device. The transfer function $H_{12}(f)$ also includes a contribution from the $+1$ order diffracted from switching segment f_C (labeled C_{+1}), which is of no consequence, as explained later.

At port 3, intended for subchannel C, the transfer function $H_{13}(f)$ includes passbands from the 0 order diffracted from switching segment f_C (labeled C_0) and the $+1$ order diffracted from switching segment f_B (labeled B_{+1}). The combined passband exhibits significant rolloff at the upper nominal band edge at $f - f_B = 75$ GHz, but no rolloff until far below the lower nominal band edge at $f - f_B = 25$ GHz. The passband exhibits an additional insertion loss of $-10 \log_{10} 3 = -4.8$ dB, caused by the splitting into three equal-intensity diffraction orders. At port 4, intended for subchannel B, the transfer function $H_{14}(f)$ includes contributions from three overlapping diffraction orders (labeled C_{-1} , B_0 , and A_{+1}), and exhibits no rolloff until far below and above the nominal lower and upper band edges at $f - f_B = -25$ and 25 GHz, respectively. Finally, port 5, intended for subchannel A, operates as a mirror image of port 3 with respect to $f - f_B = 0$.

Fig. 6 shows the (sub)channels demultiplexed at node 3 in Fig. 1. Given the 10-GHz guard bands at the upper and lower edges of narrow-band channel D, the upper edge of subchannel C, and the lower edge of subchannel A, all of the (sub)channels appear at the desired drop ports with negligible distortion. Although additional (sub)channels appear at the drop ports (e.g., subchannels A and C appear along with desired subchannel B at port 4), these are orthogonal to the desired (sub)channels, and are filtered effectively by digital OFDM demodulation, as explained in Section III-B.

At each drop port, the multiple diffraction orders can potentially interfere constructively or destructively at frequencies

where they overlap, leading to nonflat passbands. To prevent such interference, the average square-wave phase Φ_0 has an additive phase shift alternating between 0 and $\pi/2$ in adjacent SLM switching segments, and the square-wave spatial phase shift φ_g has an additive phase shift alternating between 0 and π (half a period) in adjacent SLM switching segments. The phases Φ_0 and φ_g are described in the top panel of in Fig. 4.

Figs. 4 and 5 assume the following design parameters. Input and output fibers are collimated using a linear lens array of focal length 2.6 mm. The ruled grating has 1200 1 p/mm, operates at an 85° angle of incidence, and has an angular dispersion $\partial\theta/\partial f = 1.91 \times 10^{-5}$ rad/GHz. The Fourier lens has a focal length $f_{\text{lens}} = 150$ mm. The phase-only LCOS SLM has 512×512 pixels, each $15 \times 15 \mu\text{m}$ in size. Using (2) with $\Delta v = 50$ GHz, the switching segment width should be $w_{\text{seg}} = 143 \mu\text{m}$ (9.5 pixels)² along the f dimension in Fig. 3. A monochromatic input signal forms a spot on the SLM of dimensions $108 \mu\text{m} \times 624 \mu\text{m}$ along the f and x dimensions in Fig. 3, respectively. Splitting into three diffraction orders is achieved by imposing a square-wave phase grating on the SLM with an amplitude equal to 2.03 radians and period equal to $120 \mu\text{m}$ (8 pixels), which gives a first-order diffraction angle of $\alpha_{\text{sw}} = 12.9$ mrad. Using (3), the spacing between collimated beams at adjacent add/drop ports is 1.94 mm. Fig. 5 was computed with the LCOS SLM discretized into a mesh of 1024×1024 samples (2×2 samples per pixel).

In this WSS design, the number of add/drop ports is limited by the number of addressable fiber ports in the linear input/output array. For example, 1×9 devices are commercially available (one input or output port and eight add or drop ports), and such a configuration could support wideband channels up to 8×50 GHz. The number of add/drop ports can be increased by increasing the WSS dimensions or altering its design [13].

III. OFDM SYSTEM DESIGN

The proposed network architecture can be realized using either SC modulation or CO-OFDM, given appropriate synchronization between cooperating transceivers. In this section, assuming CO-OFDM, we analyze performance in the presence of several impairments, including fiber dispersion, aliasing, symbol synchronization errors, and phase and frequency synchronization errors. We establish design requirements, particularly for synchronization between cooperating transceivers. We present an exemplary system design, evaluating its performance in nonlinear fiber transmission.

A. Cyclic Prefix

Linear impairments in single-mode fiber (SMF) transmission include group-velocity dispersion (GVD) and polarization-mode dispersion (PMD). To avoid ISI, the cyclic prefix length should be equal to the duration of the overall system impulse response [16]. Considering only GVD, the required

²In simulation, subpixel sampling allows one to use fractional pixels in the f dimension. In practice, only whole pixels can be used, in which case, the focal length of the Fourier lens and/or the dispersion of the grating can be adjusted so that 50-GHz switching segments utilize an integral number of pixels.

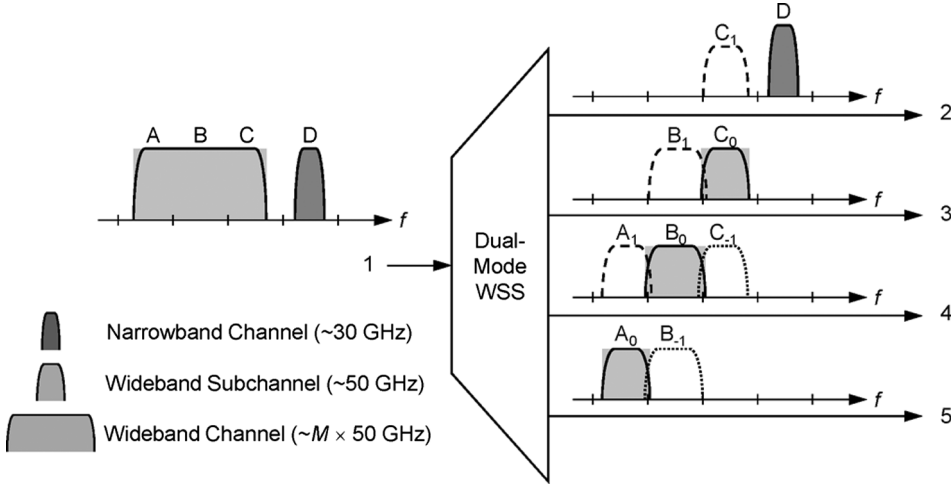


Fig. 6. Demultiplexing of narrow-band and wideband channels at node 3 of Fig. 1 by dual-mode WSS. Diffraction orders $n = -1, 0$, and $+1$ are represented as dotted, solid, and dashed lines, respectively. Subscripted labels denote the orders diffracted from the switching segments. For example, C_1 denotes the $+1$ order diffracted from switching segment f_C .

number of cyclic prefix samples (referred to a unit oversampling ratio) can be estimated as

$$N_{\text{cp}} = \frac{2\pi B_{\text{sub}}(\beta L)_{\text{net}}}{T_s} \quad (4)$$

where B_{sub} is the used bandwidth of the (sub)channel, $(\beta L)_{\text{net}}$ is the net uncompensated GVD, and T_s is the sampling interval (without oversampling) [16], which is given by $T_s = 1/R_s$, where R_s is the equivalent symbol rate per polarization (assumed equal to 50 GHz). The worst case is when a subchannel uses the full bandwidth ($B_{\text{sub}} = R_s$), in which case, (4) can be simplified to

$$N_{\text{cp}} = 2\pi R_s^2 (\beta L)_{\text{net}}. \quad (5)$$

Estimating the required cyclic prefix length for PMD is normally done by simulation, since closed-form expressions for the PMD impulse or frequency response are not known. Typically, PMD requires 1 to 5 additional cyclic prefix samples [16]. Likewise, additional cyclic prefix samples are required to accommodate the receiver's antialiasing filter.

For (sub)channels using a given symbol rate and constellation size, the cyclic prefix samples represent a reduction of the bit rate by a ratio $N_u/(N_u + N_{\text{cp}})$, where N_u is the number of used subcarriers. Hence, to minimize the bit-rate loss, N_u should be chosen as high as possible.

B. Adjacent Subchannel Aliasing

Because wideband subchannels are split into three diffraction orders, at an output port of the WSS, a desired (sub)channel may be accompanied by one or two adjacent (sub)channels, as shown in Fig. 6. While the adjacent (sub)channels are nominally eliminated by antialias filtering and subsequent digital filtering, some aliasing on the desired (sub)channel can occur because of the finite rolloff rate of the antialiasing filter, as shown in Fig. 7.

The worst case aliasing occurs when a desired subchannel uses the full 50-GHz bandwidth and overlaps with two adjacent subchannels, as at output port 4 in Fig. 6. In this case, subcarrier

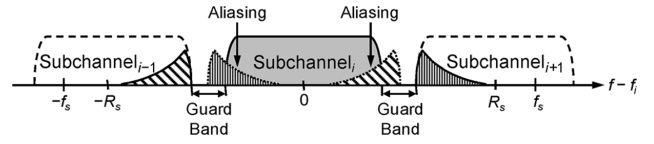


Fig. 7. Aliasing of adjacent OFDM subchannels due to the finite rolloff of the antialiasing filter when detecting subchannel i . The subchannel spacing is equal to the symbol rate, $R_s = 50$ GHz, and the sampling frequency f_s is 64 GHz.

k of subchannel i will have aliasing from subcarrier q of subchannel $i + 1$ when $f_k^i = f_q^{i+1} - f_s$, where f_s is the sampling frequency. Similarly, there will be aliasing from subchannel $i - 1$ when $f_k^i = f_l^{i-1} + f_s$. The variance of aliasing noise on subcarrier k of subchannel i is

$$\sigma_{\text{ali}}^2[k] = P_q^{i+1} |H_{\text{Rx}}(q \cdot \delta f)|_{|q=k+N_c}^2 + P_l^{i-1} |H_{\text{Rx}}(l \cdot \delta f)|_{|l=k-N_c}^2 \quad (6)$$

where P_q^{i+1} and P_l^{i-1} are the powers of subcarriers q and l of subchannels $i + 1$ and $i - 1$, respectively, $H_{\text{Rx}}(f)$ is the antialiasing filter frequency response, and δf is the subcarrier spacing. We have used the expressions $f_l^{i-1} = l \cdot \delta f$, $f_q^{i+1} = q \cdot \delta f$ and $f_s = N_c \cdot \delta f$. The SNR of subcarrier k of subchannel i is

$$\text{SNR}^i[k] = \frac{P_k^i}{\sigma_{\text{AWGN}}^2 + \sigma_{\text{ali}}^2[k]} \quad (7)$$

where σ_{AWGN}^2 is the variance of additive white Gaussian noise (AWGN) from amplified spontaneous emission (ASE). We observe in (7) that the SNR is not the same for all subcarriers. Assuming all subcarriers use PM-QPSK, the symbol-error ratio (SER) of subchannel i averaged over the subcarriers is [16]:

$$\bar{P}_s^i = \frac{1}{N_u} \sum_{k=0}^{N_u-1} 2Q(\sqrt{\text{SNR}^i[k]}) \quad (8)$$

where N_u is the number of used subcarriers and $Q(x)$ is the Gaussian Q function [17]. An alternate performance metric

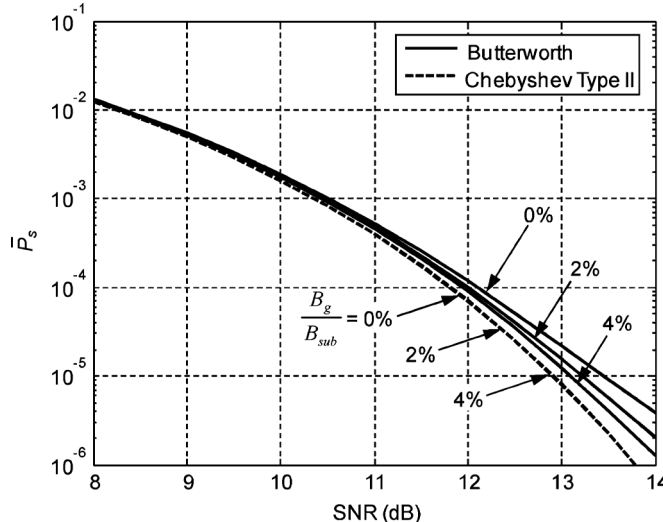


Fig. 8. OFDM SER in the presence of aliasing for different fifth-order anti-aliasing filters and normalized guard bandwidths B_g/B_{sub} . The OFDM parameters are $N_c = 128$, $N = 100$, $B_{\text{sub}} = 50$ GHz, and $M_s = 1.28$.

conveying the same information is the equivalent SNR of subchannel i , given by

$$\text{SNR}_{\text{eq}}^i = \left[Q^{-1} \left(\frac{\bar{P}_s^i}{2} \right) \right]^2 \quad (9)$$

where $Q^{-1}(x)$ is the inverse Gaussian Q function [17].

In order to minimize aliasing noise, we introduce a guard band between adjacent subchannels. By not modulating $N_g/2$ subcarriers on the upper and lower edges of a subchannel, we can create a guard bandwidth $B_g = N_g \cdot \delta f$. We define a normalized guard bandwidth

$$\frac{B_g}{B_{\text{sub}}} = \frac{N_g}{N} \quad (10)$$

where N is the number of potentially available subcarriers. The guard band reduces the bit rate, since only $N_u = N - N_g$ subcarriers are used for data transmission.

Fig. 8 shows the SER \bar{P}_s for different fifth-order antialiasing filter types and normalized guard bandwidths B_g/B_{sub} . The fast Fourier transform (FFT) size is $N_c = 128$, and $N = 100$, such that the oversampling ratio is $M_s = 1.28$. The subchannel bandwidth is $B_{\text{sub}} = 50$ GHz and $f_s = M_s B_{\text{sub}} = 64$ GHz. The 3-dB bandwidth of the antialiasing filters is equal to B_{sub} .

In Fig. 8, for the Butterworth filter, the aliasing penalty decreases as the guard bandwidth increases, but remains measurable even for $B_g/B_{\text{sub}} = 4\%$. By contrast, a Chebyshev type II filter, which has a more abrupt transition region, virtually eliminates aliasing noise. A fifth-order Chebyshev type II filter with 3-dB bandwidth equal to B_{sub} is used exclusively below.

C. Symbol Timing Synchronization

1) Transmitter: In order to maintain orthogonality between the subchannels comprising a wideband channel, all transmit symbol clocks at a node are locked to an electrical or optical clock reference, as shown in Figs. 1 and 2. To avoid clock skew, each transmitter applies a fixed de-skewing correction. Once a transmitter is plugged into a WSS input port, a calibration can

be performed *in situ* and stored in a lookup table. After calibration, a clock skew (e.g., caused by temperature gradients) can be accommodated, up to a maximum of $T_s = 1/R_s = 20$ ps. If necessary, any additional clock skew can be accommodated by appending additional cyclic samples in the prefix or in a suffix, which is known as the Zipper method [18].

2) Receiver: Receiver symbol clocks can be locked to the same reference as the transmit clocks, making sampling frequency errors negligible. Symbol boundaries can be estimated using known techniques, such as transmitting a training preamble [19]–[21] or using the redundancy in the cyclic prefix [22].

D. Phase and Frequency Synchronization

When phase and frequency errors are present, we can write the received signal $y(t)$ for one subchannel as

$$y(t) = \left[e^{j2\pi\Delta f_{\text{Rx}}t + j\theta_{\text{Rx}}(t)} \cdot \left(w(t) e^{j2\pi\Delta f_{\text{Tx}}t + j\theta_{\text{Tx}}(t)} * h_{\text{fiber}}(t) \right) \right] * h_{\text{Rx}}(t) \quad (11)$$

where $w(t)$ is the transmitted subchannel waveform, $h_{\text{fiber}}(t)$ and $h_{\text{Rx}}(t)$ are the impulse responses of the fiber and the antialiasing filter, respectively, Δf_{Tx} and Δf_{Rx} are the frequency-locking errors of the transmitter and receiver lasers, respectively, and $\theta_{\text{Tx}}(t)$ and $\theta_{\text{Rx}}(t)$ are the random phase fluctuations of the transmitter and receiver lasers, respectively. The laser phase fluctuations and $\theta_{\text{Tx}}(t)$ and $\theta_{\text{Rx}}(t)$ can each be modeled as Wiener processes with zero mean and independent Gaussian increments with variance $\sigma^2(\Delta t) = 2\pi\beta\Delta t$, where β is the laser linewidth. To simplify the analysis, it is common to combine the receiver and transmitter phase fluctuations into a single Wiener process at the receiver [23]. A similar approximation is used for the laser frequency errors. The received signal simplifies to

$$y(t) = \left[e^{j2\pi\Delta ft + \theta(t)} \cdot (w(t) * h_{\text{fiber}}(t)) \right] * h_{\text{Rx}}(t) \\ = \left[e^{j2\pi\Delta ft + \theta(t)} \cdot x(t) \right] * h_{\text{Rx}}(t) \quad (12)$$

where $\theta(t) = \theta_{\text{Tx}}(t) + \theta_{\text{Rx}}(t)$, $\Delta f = \Delta f_{\text{Tx}} + \Delta f_{\text{Rx}}$, and $x(t) = w(t) * h_{\text{fiber}}(t)$.

1) Receiver Frequency: We assume that the local laser oscillator (LO) is frequency-locked to the desired subchannel, but with a frequency error Δf . This frequency error can be compensated, for example, by using training symbols [20] or subcarrier pilots [21] to estimate the frequency offset and then applying digital frequency correction. An alternative is to transmit an unmodulated pilot in the middle of the OFDM spectrum and then use the pilot in an analog or digital feedforward correction scheme [19].

Neglecting for now the antialiasing filter, the received subchannel i , $y^i(t)$, with LO frequency error Δf_i is given by

$$y^i(t) = e^{j2\pi\Delta f_i t} \cdot x^i(t). \quad (13)$$

After sampling the signal with sampling period $T = 1/f_s$, we obtain $y^i[n] = e^{j2\pi\Delta f_i n T} \cdot x^i[n]$. The received signal after the FFT is

$$Y^i[k] = \sum_{r=-N_c/2}^{N_c/2-1} C^i[k-r] X^i[r] \quad (14)$$

where N_c is the FFT size, $X^i[k] = \text{FFT}\{x^i[n]\}$ and $C^i[k] = \text{FFT}\{e^{j2\pi\Delta f_i nT}\}$. We can expand $Y^i[k]$ as

$$Y^i[k] = C^i[0]X^i[k] + \sum_{r=-N_c/2, r \neq k}^{N_c/2-1} C^i[k-r]X^i[r]. \quad (15)$$

In (15), we observe that all subcarriers are scaled and rotated by $C^i[0]$, and that there is ICI since the subcarriers are no longer orthogonal. The ICI variance $\sigma_{\text{ICI}}^2[k]$ on subcarrier k is

$$\sigma_{\text{ICI},i}^2[k] = \sum_{r=-N_c/2, r \neq k}^{N_c/2-1} E[C^i[k-r]^2]P_r^i \quad (16)$$

where P_r^i is the power of subcarrier r and

$$E[C^i[k]^2] = \frac{1}{N_c^2} \frac{2 - 2 \cos(2\pi(k - \Delta f_i T N_c))}{2 - 2 \cos(2\pi/N_c(k - \Delta f_i T N_c))}. \quad (17)$$

We note that the ICI is not white, i.e., the ICI variance in (16) is different for each subcarrier. We have not included the antialiasing filter in our analysis thus far. For small frequency errors, we can simplify the calculations by interchanging the filter and the frequency offset operations, rewriting (13) as

$$y^i(t) \approx e^{j2\pi\Delta f_i t} \cdot z^i(t) \quad (18)$$

where $z(t) = x(t) * h_{\text{Rx}}(t)$ and $h_{\text{Rx}}(t)$ is the antialiasing filter impulse response. The analysis is exactly the same as before except that we substitute $X[k]$ by $Z[k] = X[k] \cdot H_{\text{Rx}}[k]$. Including ASE noise, the SNR on subcarrier k is given by

$$\begin{aligned} \text{SNR}^i[k] &= \frac{E[C^i[0]^2]P_k^iH_{\text{Rx}}^2[k]}{\sigma_{\text{AWGN}}^2 + \sum_{r=-N_c/2, r \neq k}^{N_c/2-1} E[C^i[k-r]^2]P_r^iH_{\text{Rx}}^2[r]} \\ &\approx \frac{E[C^i[0]^2]P_k^iH_{\text{Rx}}^2[k]}{\sigma_{\text{AWGN}}^2 + \sum_{r=-N_c/2, r \neq k}^{N_c/2-1} E[C^i[k-r]^2]P_r^iH_{\text{Rx}}^2[r]} \end{aligned} \quad (19)$$

Fig. 9 shows the OFDM SER \bar{P}_s in the presence of LO frequency-locking errors when detecting subchannel i . The OFDM parameters are $N_c = 128$, $N = 100$, $B_g/B_{\text{sub}} = 2\%$ ($N_u = 98$), the antialiasing filter is a fifth-order Chebyshev II, and $B_{\text{sub}} = 50$ GHz.

In order to make our results independent of the number of subcarriers, the frequency error on subchannel i , Δf_i , is normalized by the subcarrier spacing δf . In Fig. 9, we used maximum likelihood (ML) estimation to estimate the phase of $C^i[0]$, which is the common phase error (CPE) of all subcarriers. Furthermore, we used all subcarriers in the ML estimation, so Fig. 9 represents the best performance achievable with CPE correction.

In Fig. 9, we compute \bar{P}_s using three different methods: analytically [using (19) and (9)], from the received SNR [using (8)], and by counting errors in Monte Carlo simulation.

In Fig. 9, by comparing \bar{P}_s obtained analytically with \bar{P}_s computed from the measured SNR, we conclude that (19) predicts the SNR on each subcarrier accurately. When comparing with \bar{P}_s obtained from simulation, however, we observe small differences because the ICI is not Gaussian-distributed. In Fig. 9, we also observe that the OFDM signal is very sensitive to receiver frequency errors.

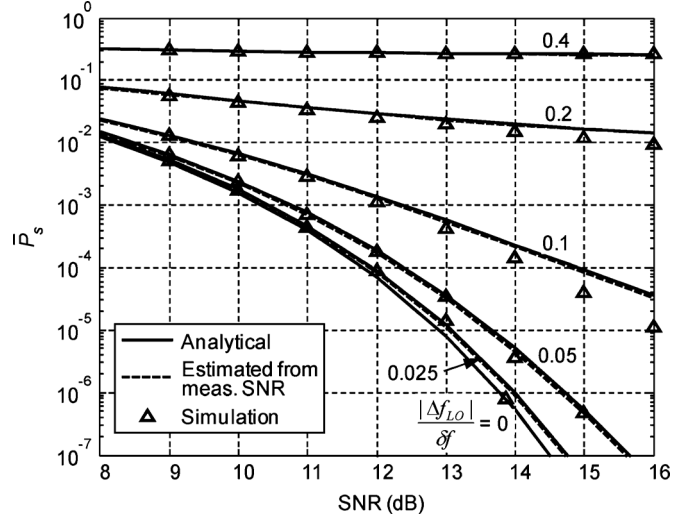


Fig. 9. OFDM SER in the presence of LO frequency-locking errors when detecting the desired subchannel i . The OFDM parameters are $N_c = 128$, $N = 100$, $B_{\text{sub}} = 50$ GHz, and $B_g/B_{\text{sub}} = 2\%$ ($N_u = 98$); the antialiasing filter is a fifth-order Chebyshev II and all subcarriers are modulated using QPSK. The normalized LO frequency errors are indicated in the figure.

2) *Transmitter Frequency*: In the proposed system, all transmit lasers are frequency-locked to a frequency comb [24], [25], as shown in Fig. 1. Such a comb can be obtained by phase modulation of light from a seed laser in an amplified recirculating loop [24]. The accuracy of each transmit laser frequency is determined by three factors: the absolute frequency accuracy of the seed, the accuracy of the comb frequency spacing, and the accuracy of locking each laser to the comb frequency. The seed is assumed locked to an absolute frequency reference (e.g., an etalon) with an accuracy of order 1 GHz [25]. This error should have negligible impact, since all subchannels within a wideband channel share a common reference comb and this error is much less than the 10-GHz guard band between channels. The spacing between comb frequencies is determined by the oscillator driving the phase modulator [24], so this error should have negligible impact (see the design example in Section III-E). The dominant errors arise from locking each transmit laser to a comb frequency, since such errors can cause interference to the desired subchannel and the adjacent subchannels appearing at the same WSS output port. Fig. 10 shows the worst case scenario when there are frequency-locking errors on the transmit lasers of the adjacent subchannels.

Assuming that the LO can lock perfectly to the desired subchannel (i), assuming, for now, that only one adjacent subchannel ($i-1$) is present, and interchanging the antialiasing filter and the frequency offset operations as above, the received electrical signal can be written as

$$y^i[n] \approx z^i[n] + e^{j2\pi\Delta f_{i-1}nT} \cdot z^{i-1}[n] \quad (20)$$

where Δf_{i-1} is the frequency-locking error on subchannel $i-1$. Using the same analysis as before, we can write the received power on subcarrier k of subchannel i as

$$\begin{aligned} E[Y^i[k]^2] &= P_k^iH_{\text{Rx}}^2[k] \\ &+ \sum_{r=-N_c/2}^{N_c/2-1} E[C^{i-1}[k-r]^2]E[Z^{i-1}[r]^2] \end{aligned} \quad (21)$$

where $C^{i-1}[k]$ is given by (17). Note that $X^{i-1}[k] = 0$ for $-N/2 \leq k \leq N/2$. However, there could be aliasing products at those subcarrier locations (see Fig. 7), depending on the frequency response of the antialiasing filter employed. Hence, $E[Z^{i-1}[k]^2]$ becomes

$$E[Z^{i-1}[r]^2] \approx \begin{cases} P_r^{i-1} H_{\text{Rx}}^2[r], & -N_c/2 \leq r \leq -N/2 + 1 \\ \sigma_{\text{ali}}^2[r], & -N/2 \leq r \leq N/2. \end{cases} \quad (22)$$

where P_r^{i-1} is the power of subcarrier r of interfering subchannel $i-1$ and $\sigma_{\text{ali}}^2[r]$ is given by (6). From (21), we can write the cross ICI variance from interfering subchannel $i-1$ as

$$\sigma_{XCI,i-1}^2 \approx \sum_{r=-N_c/2}^{N_c/2-1} E[C^{i-1}[k-r]^2] E[Z^{i-1}[r]^2]. \quad (23)$$

We also need to take into account the ICI contribution from the other interfering adjacent subchannel ($i+1$). Using the same analysis as above for interferer $i-1$, the cross ICI variance from interfering subchannel $i+1$ is given by

$$\sigma_{XCI,i+1}^2 \approx \sum_{r=-N_c/2}^{N_c/2-1} E[C^{i+1}[k-r]^2] E[Z^{i+1}[r]^2] \quad (24)$$

where

$$E[Z^{i+1}[r]^2] \approx \begin{cases} \sigma_{\text{ali}}^2[r], & -N/2 \leq r \leq N/2 \\ P_r^{i+1} H_{\text{Rx}}^2[r], & N/2 + 1 \leq r \leq N_c/2 - 1. \end{cases} \quad (25)$$

Assuming independent transmitted symbols for each interfering subchannel, the SNR of subcarrier k of subchannel i in the presence of aliasing and frequency errors on two adjacent subchannels becomes

$$\text{SNR}^i[k] \approx \frac{P_k^i H_{\text{Rx}}^2[k]}{\sigma_{\text{AWGN}}^2 + \sigma_{XCI,i-1}^2[k] + \sigma_{XCI,i+1}^2[k]}. \quad (26)$$

We note that in (26), the aliasing interference is already included in the cross ICI variances so we do not need to include the aliasing variance from (6).

An option to mitigate interference from frequency errors on adjacent subchannels is to introduce a guard band between subchannels. Fig. 11 shows the equivalent SNR, SNR_{eq} , in the presence of frequency errors on the adjacent subchannels. The frequency errors are $\Delta f_{i-1} = -\Delta f_{i+1}$, such that both adjacent subchannels move towards the desired subchannel i , as shown in Fig. 10. The OFDM parameters are $N_c = 128$, $N = 100$, $B_{\text{sub}} = 50$ GHz, and $B_g/B_{\text{sub}} = 2\%$ ($N_u = 98$). We use a fifth-order Butterworth anti-aliasing filter in Fig. 11 in order to better illustrate aliasing effects.

In Fig. 11, we observe that the analytical approach is able to estimate the subcarriers SNRs with reasonable accuracy. We also observe that the interference from the adjacent subchannels is periodic, and is worst when the frequency errors are an odd integer multiple of half the subcarrier spacing. When the frequency errors are an integer multiple of the subcarrier spacing, there is no interference. We further observe that the interference

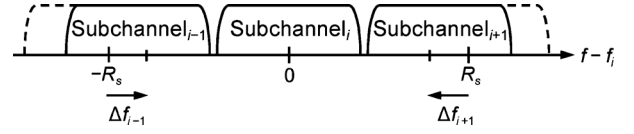


Fig. 10. Worst case scenario when there are frequency-locking errors in the locking of the adjacent transmit lasers to the frequency reference comb.

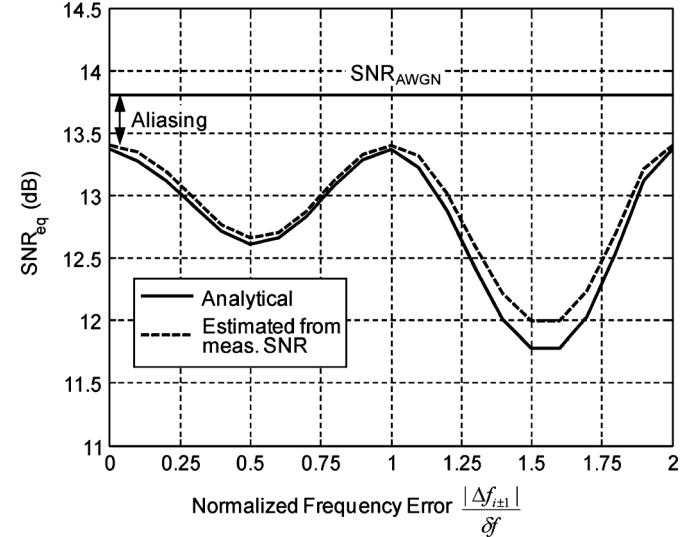


Fig. 11. OFDM equivalent SNR in the presence of frequency errors on the transmit lasers of the adjacent subchannels. The frequency errors are $\Delta f_{i-1} = -\Delta f_{i+1}$, such that both adjacent subchannels move toward the desired subchannel i , as shown in Fig. 10. The OFDM parameters are $N_c = 128$, $N = 100$, $B_{\text{sub}} = 50$ GHz, and $B_g/B_{\text{sub}} = 2\%$ ($N_u = 98$); the antialiasing filter is a fifth-order Butterworth and all subcarriers are modulated using QPSK.

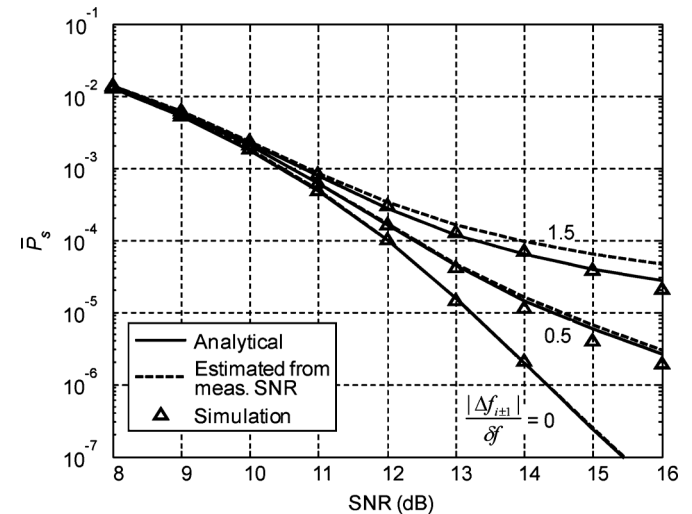


Fig. 12. OFDM SER \bar{P}_s in the presence of frequency errors on the transmit lasers of the adjacent subchannels. The frequency errors are $\Delta f_{i-1} = -\Delta f_{i+1}$, such that both adjacent subchannels move towards the desired subchannel i . The OFDM parameters are the same as in Fig. 11 and the frequency errors normalized to the subcarrier spacing δf are indicated in the figure.

becomes worse as the adjacent subchannels move closer to the desired subchannel.

Fig. 12 shows the OFDM SER \bar{P}_s for the same configuration as in Fig. 11. We observe small differences between the \bar{P}_s obtained from simulation and from the subcarriers SNRs (whether

measured or computed analytically), because the cross ICI is not Gaussian.

By comparing Fig. 12 to Fig. 9, we conclude that performance is more sensitive to frequency-locking errors of the LO than those of the transmit lasers.

3) *Transmitter and Receiver Phase Noise*: Neglecting frequency errors and using the same approximations as above, the received signal can be written as

$$y^i[n] \approx e^{j\theta_i[n]} \cdot z^i[n] + e^{j\theta_{i-1}[n]} \cdot z^{i-1}[n] + e^{j\theta_{i+1}[n]} \cdot z^{i+1}[n] \quad (27)$$

where $\theta_i[n]$ is the phase noise of subchannel i . We note that the above simplification is only valid for systems with small accumulated dispersion [26]. Using the same analysis as above, the received power on subcarrier k of subchannel i can be written as

$$E[Y^i[k]^2] = E[I_m^i[0]^2] P_k^i H^2[k] + \sigma_{PN,i}^2[k] + \sigma_{PN,i+1}^2[k] + \sigma_{PN,i-1}^2[k] \quad (28)$$

where $\sigma_{PN,i}^2$ is the phase variance on subchannel i , given by

$$\sigma_{PN,i}^2[k] = \sum_{r=-N_c/2}^{N_c/2-1} E[I_m^i[k-r]^2] E[Z^i[r]^2]. \quad (29)$$

$E[I_m[k]^2]$ is equal to [23]

$$E[I_m^i[k]^2] = \frac{1}{N_c^2} \left\{ 2\Re \left(\frac{d_{k,i}^{N_c+1} - (N_c+1)d_{k,i} + N_c}{(d_{k,i}-1)^2} \right) - N_c \right\} \quad (30)$$

where $d_{k,i} = \exp(j2\pi k/N_c - \pi\beta_i T)$ [23]. We recall that $E[Z^i[k]^2] = P_k^i H_{Rx}^2[k]$ and $E[Z^{i\mp 1}[k]^2]$ are given by (22) and (25), respectively.

Assuming independent transmitted symbols for each subchannel, the SNR of subcarrier k of subchannel i in the presence of phase noise becomes

$$\text{SNR}^i[k] \approx \frac{E[I_m^i[0]^2] P_k^i H_{Rx}^2[k]}{\sigma_{AWGN}^2 + \sigma_{PN,i}^2[k] + \sigma_{PN,i-1}^2[k] + \sigma_{PN,i+1}^2[k]}. \quad (31)$$

Fig. 13 shows the equivalent SNR as a function of the laser linewidth β , assuming all lasers have the same linewidth.

We observe that, for a given number of subcarriers, the SNR decreases as the laser linewidth increases. Furthermore, we verify that the SNR degradation is more significant as the number of subcarriers increases.

Fig. 14 shows the OFDM SER \bar{P}_s for various laser linewidths. In order to make the results independent of number of subcarrier, we use the normalized linewidth [23]

$$\frac{N \cdot \beta}{B} = \frac{\beta}{\delta f}. \quad (32)$$

The OFDM parameters are $N_c = 256$, $N = 200$, $B_{\text{sub}} = 50$ GHz, and $B_g/B_{\text{sub}} = 1\%$ ($N_u = 198$) and the antialiasing filter is a fifth-order Chebyshev II. We assumed that all lasers

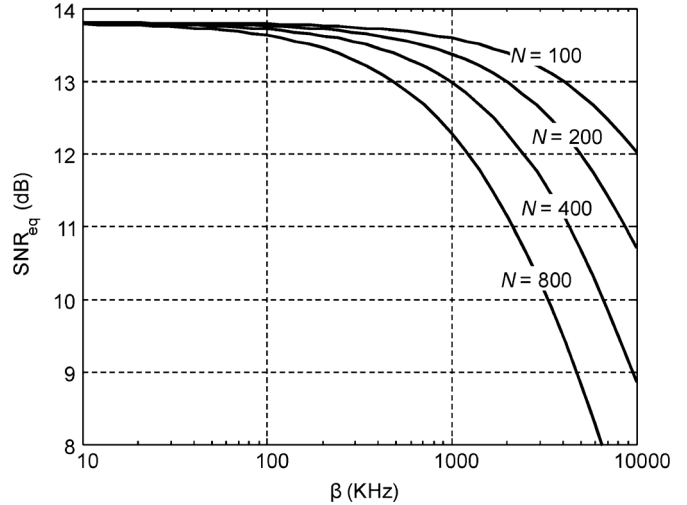


Fig. 13. OFDM equivalent SNR as a function of the laser linewidth β . The system parameters are $B_{\text{sub}} = 50$ GHz and $B_g/B_{\text{sub}} = 2\%$; the antialiasing filter is a fifth-order Chebyshev II and all subcarriers are modulated using QPSK. The number of subcarriers N is indicated in the figure.

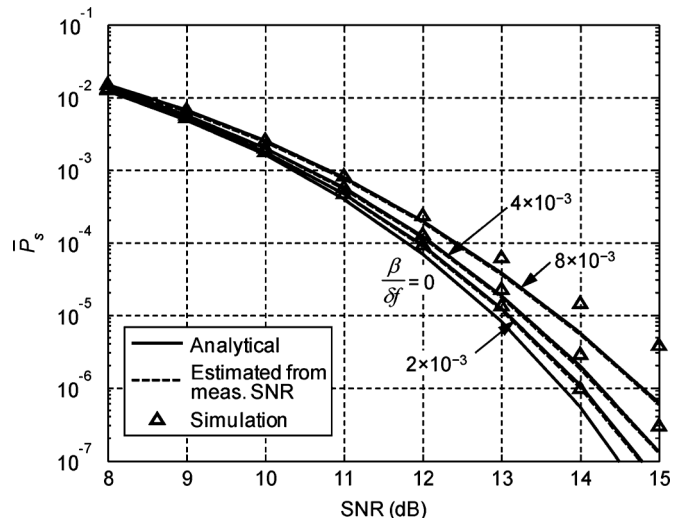


Fig. 14. OFDM SER \bar{P}_s for various laser linewidths. The OFDM parameters are $N_c = 256$, $N = 200$, $B_{\text{sub}} = 50$ GHz, and $B_g/B_{\text{sub}} = 1\%$ ($N_u = 198$); the antialiasing filter is a fifth-order Chebyshev II and all subcarriers are modulated using QPSK. The laser linewidths normalized to the subcarrier spacing δf are indicated in the figure.

have the same linewidth. We used ML estimation of the CPE of all subcarriers. All subcarriers were used in the ML estimation, such that Fig. 14 represents the best performance achievable with CPE correction.

In Fig. 14, we verify that (31) correctly estimates the SNR of each subcarrier. We observe, however, that the \bar{P}_s obtained using these subcarrier SNRs does not match with simulation results for high linewidths. This occurs because the phase noise does not have Gaussian statistics, and also because of SER floors that become dominant at high linewidths, as observed in [27]. Using simulations, we have found that an SER floor of $\bar{P}_s < 5 \times 10^{-7}$ for QPSK corresponds to a normalized laser linewidth of $\beta/\delta f < 1 \times 10^{-2}$. As long as the target \bar{P}_s is significantly higher than the SER floor, \bar{P}_s can be estimated accurately using the subcarrier SNRs.

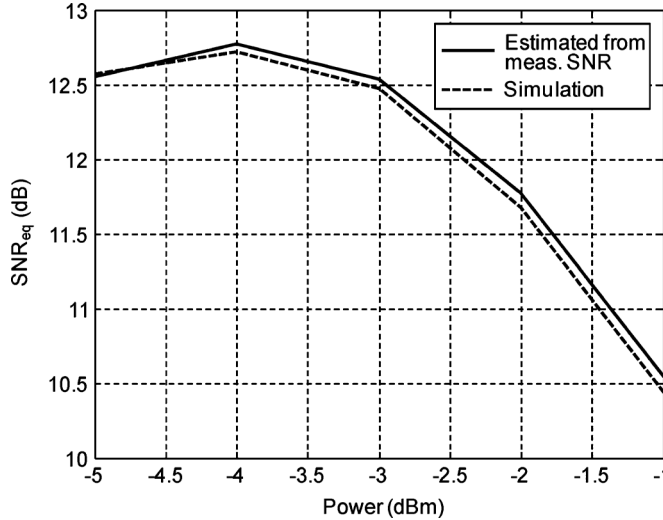


Fig. 15. Equivalent SNR versus launched power of a single-subchannel dual-polarization OFDM system in the presence of fiber nonlinearity after $N_A = 19$ spans of propagation ($L = 1520$ km) with 10% RDPS. The OFDM parameters are $N_c = 1024$, $N = 800$, $N_{cp} = 53$, $B_{sub} = 50$ GHz, and $B_g/B_{sub} = 0.5\%$ ($N_u = 796$).

E. OFDM Design Example

The reach of a long-haul system is ultimately limited by ASE and fiber nonlinearity. OFDM system reach is maximized typically by choosing 100% residual dispersion per span (RDPS), because four-wave mixing is reduced by an accumulated phase mismatch between the subcarriers [28], and because elimination of the dispersion-compensating fiber (DCF) (and the accompanying optical amplifiers) eliminates sources of nonlinearity and noise. The choice of 100% RDPS requires an extremely long cyclic prefix, which then requires a large number of subcarriers to minimize the prefix overhead, making a system more sensitive to synchronization errors. In this study, we have chosen 10% RDPS as a compromise between nonlinear performance and synchronization requirements.

Fig. 15 shows the equivalent SNR versus launched power of a single-subchannel dual-polarization OFDM system in the presence of fiber nonlinearity after propagating through $L = 1520$ km of SMF. The system parameter values are typical of dispersion-managed terrestrial links: $N_A = 19$ spans, $L_{SMF} = 80$ km, $\alpha_{SMF} = 0.22$ dB/km, $D_{SMF} = 17$ ps/nm-km, $\gamma_{SMF} = 1.2$ W $^{-1}$ /km, $\alpha_{DCF} = 0.6$ dB/km, $D_{DCF} = -85$ ps/nm-km, and $\gamma_{DCF} = 5.3$ W $^{-1}$ /km. Amplifiers with spontaneous emission factor $n_{sp} = 1.41$, and gains G_1 and G_2 are placed after each span of SMF and each DCF, respectively, with total gain compensating the total span loss, and with optimized gain ratio $G_2/G_1 = 2.1$.

The OFDM and synchronization parameters for the system design example are summarized in Tables I and II, respectively.

The results in Fig. 15 do not include the effects of the phase and frequency errors discussed in Section III-D.

In Fig. 15, we observe that the optimal trade-off between ASE noise and nonlinearity is obtained at an optimal launched power of -4 dB·m. We also verify in Fig. 15 that the performance estimated from the subcarrier SNRs matches closely with the simulated SNR. The nonlinear distortion on each subcarrier is approximately Gaussian because, after the FFT, it is the sum many

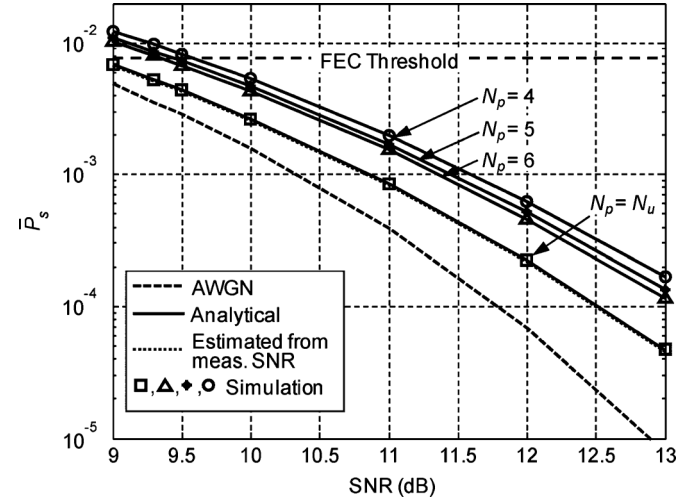


Fig. 16. OFDM SER \bar{P}_s versus SNR in the presence of frequency-locking errors and laser phase noise. The LO residual frequency error is $\Delta f_i = 3.125$ MHz and the frequency-locking errors at the transmit lasers are $\Delta f_{i+1} = \pm 31.25$ MHz. All lasers have a linewidth $\beta = 50$ kHz. The OFDM parameters are $N_c = 1024$, $N = 800$, $N_{cp} = 53$, $B_{sub} = 50$ GHz, and $B_g/B_{sub} = 0.5\%$ ($N_u = 796$). The antialiasing filter is a fifth-order Chebyshev II and all subcarriers are modulated using QPSK. The number of pilots N_p used for CPE correction is indicated in the figure.

TABLE I
OFDM PARAMETER VALUES FOR THE DESIGN EXAMPLE

Equivalent symbol rate R_s	50 GHz
Sampling rate f_s	64 GHz
Oversampling ratio $M_s = f_s/R_s$	1.28
Anti-aliasing filter	25 GHz, Fifth-order Chebyshev II
Subcarrier spacing δf	62.5 MHz
Frequency correction accuracy	± 3.1 MHz
Cyclic prefix (at 1 sample/symbol)	53
FFT / IFFT size N_c	1024
Possible subcarriers N_c/M_s	800
Guard subcarriers N_g	2 + 2
Used subcarriers N_u	796
Pilot subcarriers N_p	6 (including 1 at d.c.)
Data-bearing subcarriers	791

TABLE II
SYNCHRONIZATION PARAMETER VALUES FOR THE DESIGN EXAMPLE

Tx clock synchronization accuracy	± 10 ps
Tx comb absolute accuracy	± 1 GHz
Tx comb spacing accuracy	± 500 kHz
Tx and LO frequency locking accuracy	± 31.3 MHz
Tx and LO laser linewidth	50 kHz

approximately independent, identically distributed random variables, and because of the interaction of nonlinearity with GVD.

In Fig. 15, the single OFDM subchannel has an equivalent SNR of 12.7 dB after propagating 1520 km. If fiber nonlinearity were not present, the received SNR would be 14.7 dB, so the intrachannel nonlinear penalty is estimated to be 2 dB. The intrachannel nonlinear penalty estimated to be 2 dB for 10% RDPS [29]. Hence, excluding the effects of phase and frequency synchronization errors, the SNR is estimated to be $12.7 - 2 = 10.7$ dB after 1520 km.

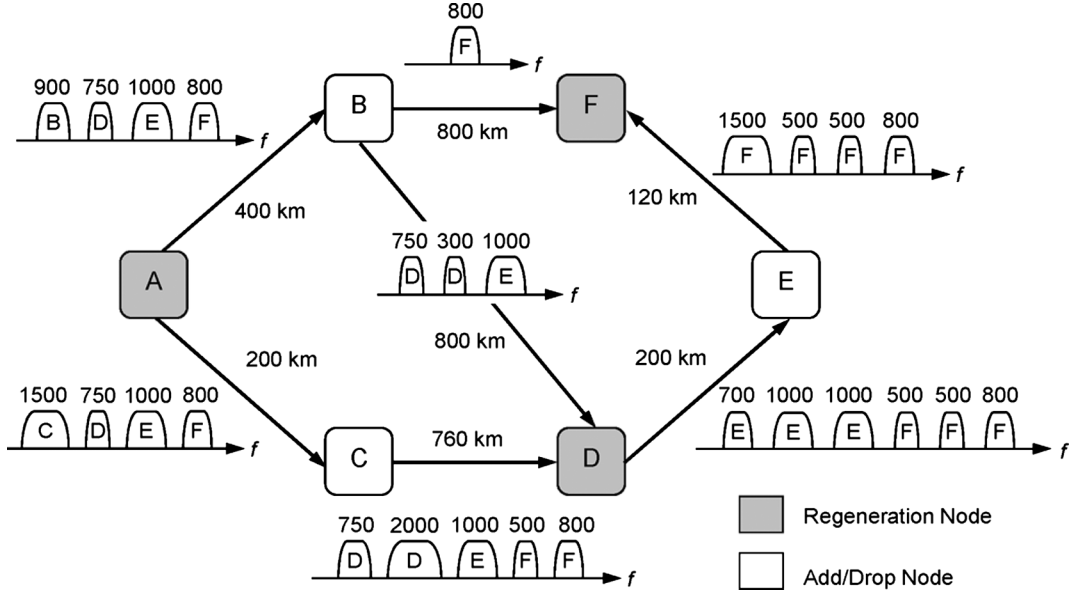


Fig. 17. Traffic routes and demands in a network at a particular time. Demands are labeled by bit rate (in Gbit/s) and destination node.

From Fig. 9, we aim for a maximum residual LO frequency error (after digital frequency correction) of $\Delta f_{\text{LO}} = 0.05f$, corresponding to 3.125 MHz for the assumed OFDM design. From Fig. 12, we set the maximum frequency-locking error at the transmit lasers to $\Delta f_{i-1} = -\Delta f_{i+1} = 0.5\delta f$, which corresponds to 31.25 MHz. From Fig. 14, we choose a maximum combined linewidth $\beta < 2 \times 10^{-3}\delta f$, which corresponds to a laser linewidth of 50 kHz. For the comb generator, we choose a crystal accuracy of 10 pm for the 50-GHz oscillator, which sets the comb spacing accuracy within 500 kHz. The comb absolute frequency accuracy is determined by the seed laser, which typically is of the order of 1 GHz [25]. The clock synchronization error can be up to $\pm T_s$, which corresponds to ± 10 ps for our system.

In order to confirm our choice for the system parameters, in Fig. 16, we present the SER \bar{P}_s versus SNR when all the aforementioned impairments are present except for fiber nonlinearity. We assume a forward error correction (FEC) code with 7% overhead and a BER threshold $P_{b,\text{thresh}} = 3.8 \times 10^{-3}$ ($P_{s,\text{thresh}} = 7.6 \times 10^{-3}$ for QPSK) [7], [30]. The FEC threshold corresponds to $\text{SNR}_{\text{thresh}} = 8.5$ dB. In the analytical calculation of \bar{P}_s in Fig. 16, we have estimated the SNR of subcarrier k of subchannel i as

$$\text{SNR}^i[k] \approx \frac{E[C^i[0]^2]E[I_m^i[0]^2]P_k^iH_{\text{RX}}^2[k]}{\sigma_{\text{AWGN}}^2 + \sum_{\text{all impairments}}\sigma_{\text{ICI}}^2[k]} \quad (33)$$

where the sum in the denominator is over all impairments except fiber nonlinearity. A more exact calculation could be done by using (29)–(31) with $d_{k,i} = \exp(j2\pi(k - \Delta f_i TN_c)/N_c - \pi\beta_i T)$. However, the difference between the two approaches is negligible.

In Fig. 16, we used a number N_p subcarriers as pilots for CPE correction using ML estimation. We observe that $N_p = 6$ gives only a small SNR penalty compared to the ideal case when $N_p = N_u$. We also verify that the overall penalty relative to the

AWGN limit is 0.8 dB at $\text{SNR}_{\text{thresh}} = 8.5$ dB. Furthermore, after propagating 1520 km, excluding phase and frequency synchronization errors, the SNR is 10.7 dB, so the system margin is $10.7 - 0.8 - 8.5 = 1.4$ dB.

After selecting the OFDM parameters as in Table I, we can compute the bit rate per subchannel (excluding coding overhead) as

$$R_b^{\text{pre}} = n_{\text{pol}}b \frac{N_{\text{data}}}{N} \frac{N_c}{N_c + \lceil M_s N_{\text{cp}} \rceil} B_{\text{sub}} \quad (34)$$

where n_{pol} is the number of used polarizations, b is the number of bits per symbol, N_{data} is the number of data carrying subcarriers, and $\lceil \cdot \rceil$ is the ceiling operation. In our case, $N_{\text{data}} = N - N_g - N_p + 1 = N_u - N_p + 1$, because we employed the unused d.c. tone as pilot. Using the values in our example, we obtain $R_b^{\text{pre}} = 185.44$ Gbit/s (excluding coding overhead). Assuming a line code 64/66 and 7% FEC overhead, we obtain the maximum bit rate per subchannel $R_b^{\text{max}} = 168.54$ Gbit/s, corresponding to a spectral efficiency of 3.4 bit/s/Hz. As explained in Section II, each wideband channel has a guard band of 10 GHz on the upper and lower edges. The bit rate of a wideband channel with M subchannels is

$$R_b(M) = MR_b^{\text{max}} - \frac{20}{50}R_b^{\text{max}}. \quad (35)$$

In our network design example, we assumed a WSS with eight add/drop ports. The bit rates of the wideband channels are listed in Table III.

IV. NETWORK EFFICIENCY

In this section, we evaluate some measures of efficiency and cost comparing fixed-bandwidth networks with variable-bandwidth networks.

Fig. 17 shows routes and traffic demands in a model network, used to compare the efficiency of fixed-bandwidth networks (using only traditional 100 Gbit/s narrow-band channels)

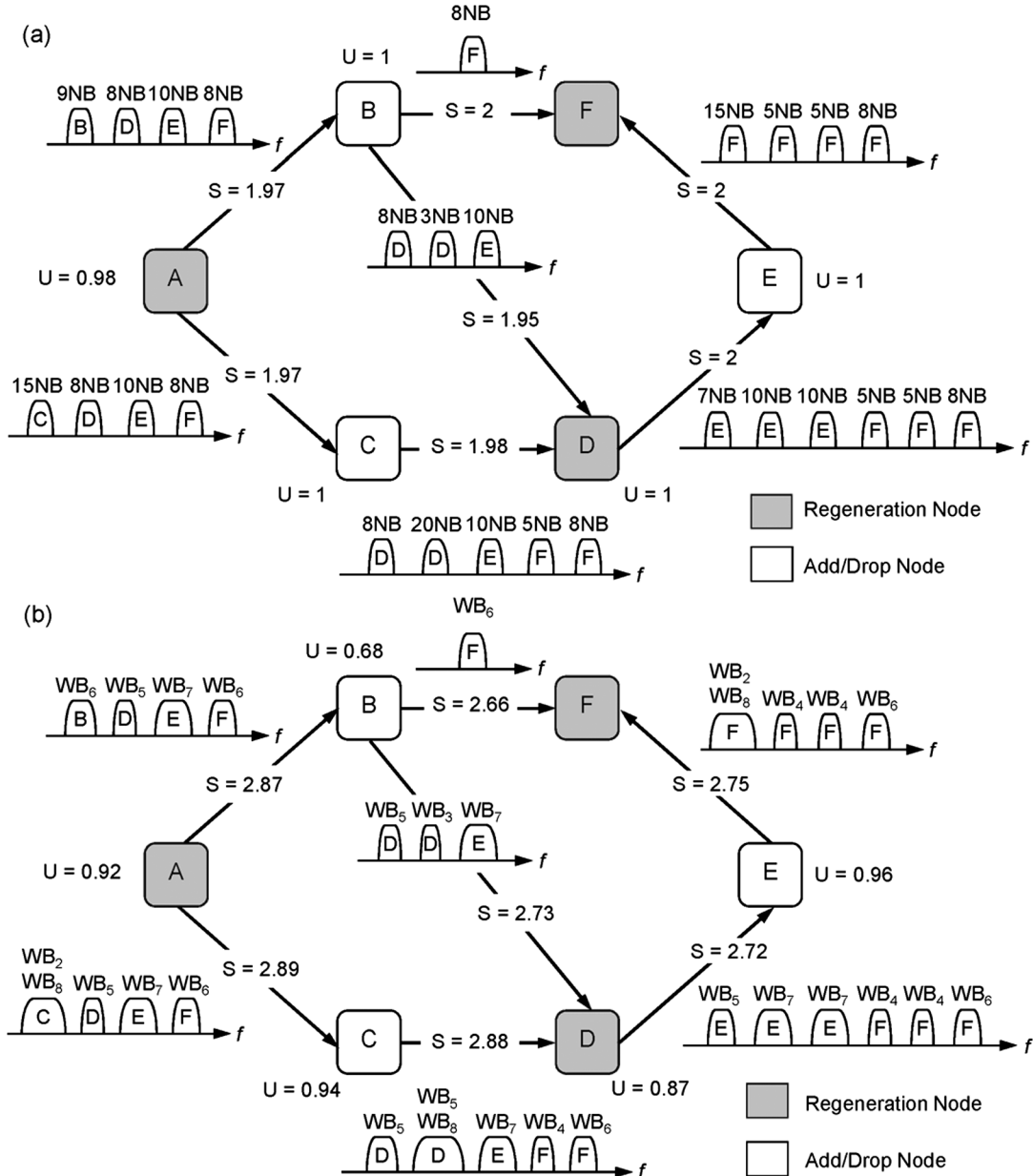


Fig. 18. Network efficiency when traffic demands in Fig. 17 are met using (a) fixed-bandwidth channels and (b) variable-bandwidth channels. The comparative figures of merit are spectral efficiency S and transceiver utilization U . The fixed-bandwidth channels transmit at 100 Gbit/s in a nominal 50-GHz bandwidth. The details of the variable-bandwidth channels are listed in Table III.

to variable-bandwidth networks (using the wideband channels described in Table III).

Our comparative figures of merit are spectral efficiency (S) and transceiver utilization (U). We define the spectral efficiency as

$$S = \frac{\text{total link bit rate}}{\text{total used bandwidth}}. \quad (36)$$

We define the transceiver utilization (U) at node j as the traffic added at node j divided by the maximum bit rate that could be added by all the transceivers in use at the node j , as given by (37)

$$U = \frac{\text{traffic added at node } j}{\text{bit rate achievable by line cards in use at node } j}. \quad (37)$$

Fig. 18(a) and (b) compares the efficiencies achieved when the traffic demands in Fig. 17 are accommodated using fixed-

TABLE III
BANDWIDTHS AND BIT RATES OF WIDEBAND CHANNELS WITH M SUBCHANNELS

Number of Subchannels M	Nominal Occupied Bandwidth (GHz)	Used Bandwidth (GHz)	Bit Rate (Gbit/s)
2	100	80	269.7
3	150	130	438.2
4	200	180	606.7
5	250	230	775.3
6	300	280	943.8
7	350	330	1112.3
8	350	330	1280.9

bandwidth and variable-bandwidth channels, respectively. Variable-bandwidth channels increase spectral efficiency from an

average of about 2 to nearly 3 bits/s/Hz. On the other hand, using variable-bandwidth channels reduces transceiver utilization from an average of nearly 1 to about 0.87. The maximum bit rate of dual-mode transceivers are not fully used unless traffic demands coincide with a sum of variable-bandwidth channel bit rates. Nevertheless, we note that the average utilization of 0.87 is far higher than that achievable using superchannels whose bit rate is fixed at a high value, such as 1 Tbit/s.

V. CONCLUSION

We proposed a flexible, scalable, and modular system architecture supporting variable-bandwidth channels to enable increased traffic aggregation and maximize spectral efficiency. In particular, the proposed network supports channel bit rates scalable from 100 Gbit/s to beyond 1 Tbit/s using technology available now or in the immediate future. The proposed architecture employs colorless dual-mode transceivers, which can operate individually to transmit/receive conventional narrow-band channels, or can cooperate to transmit/receive a wideband channel, comprising M subchannels, each with 50 GHz bandwidth. We also described an LCOS WSS design that can (de)multiplex narrow-band channels with minimal loss, or can (de)multiplex wideband channels with an additional loss not exceeding 1/3 (~ 4.8 dB) independent of M . In this architecture, in principle, the transceivers can either use SC modulation or CO-OFDM. We studied the design and performance for a CO-OFDM implementation of the architecture. The impact of various impairments, including fiber dispersion, aliasing, symbol timing errors, and carrier phase and frequency errors. We discussed the tradeoffs in the choice of OFDM parameters. We evaluated a system design example using CO-OFDM with 10% RDPS, which is capable of 1520-km reach with 1.4-dB margin above the FEC threshold. We compared fixed-bandwidth networks to variable-bandwidth networks in terms of spectral efficiency and transceiver utilization. In a model network, we observed that variable-bandwidth channels increase average spectral from about to nearly 3 bits/s/Hz, but decrease average transceiver utilization from nearly 1 to about 0.87.

REFERENCES

- [1] G. Bosco, V. Curri, A. Carena, P. Poggolini, and F. Forghieri, "On the performance of Nyquist-WDM Terabit superchannels based on PM-BPSK, PM-QPSK, PM-8QAM or PM-16QAM subcarriers," *J. Lightw. Technol.*, vol. 29, no. 1, pp. 53–61, Jan. 2011.
- [2] G. Gavioli *et al.*, "Ultra-narrow-spacing 10-channel 1.12 Tb/s D-WDM long-haul transmission over uncompensated SMF and NZDSF," *IEEE Photon. Technol. Lett.*, vol. 22, no. 19, pp. 1419–1421, Oct. 2010.
- [3] A. Sano *et al.*, "No-guard-interval coherent optical OFDM for 100-Gb/s long-haul WDM transmission," *J. Lightw. Technol.*, vol. 27, no. 16, pp. 3705–3713, Aug. 2009.
- [4] H. Masuda *et al.*, "13.5-Tb/s (135×111 -Gb/s/ch) no-guard-interval coherent OFDM transmission over 6 248 km using SNR maximized second-order DRA in the extended L-band," presented at the Opt. Fiber Commun. Conf., San Diego, CA, 2009, Paper PDPB5.
- [5] B. Zhu, X. Liu, S. Chandrasekhar, D. W. Peckham, and R. Lingle, "Ultra-long-haul transmission of 1.2-Tb/s multicarrier no-guard-interval CO-OFDM superchannel using ultra-large-area fiber," *IEEE Photon. Technol. Lett.*, vol. 22, no. 11, pp. 826–828, Jun. 2010.
- [6] S. Chandrasekhar and X. Liu, "Terabit superchannels for high spectral efficiency transmission," in *Proc. Eur. Conf. Exhib. Opt. Commun.*, 2010, pp. 1–6.
- [7] T. J. Xia *et al.*, "Field experiment with mixed line-rate transmission (112-Gb/s, 450-Gb/s, and 1.15-Tb/s) over 3 560 km of installed fiber using filterless coherent receiver and EDFA's only," presented at the Opt. Fiber Commun. Conf., Los Angeles, CA, 2011, Paper PDPA3.
- [8] J. Yu *et al.*, "Generation, transmission and coherent detection of 11.2 Tb/s (112×100 Gb/s) single source optical OFDM superchannel," presented at the Opt. Fiber Commun. Conf., Los Angeles, CA, 2011, Paper PDPA6.
- [9] Y. Ma, Q. Yang, Y. Tang, S. Chen, and W. Shieh, "1-Tb/s single-channel coherent optical OFDM transmission over 600-km SSMF fiber with subwavelength bandwidth access," *Opt. Exp.*, vol. 17, no. 11, pp. 9421–9427, 2009.
- [10] R. Dischler and F. Buchali, "Transmission of 1.2 Tb/s continuous waveband PDM-OFDM-FDM signal with spectral efficiency of 3.3 bits/s/Hz over 400 km of SSMF," presented at the Opt. Fiber Commun. Conf., San Diego, CA, p. 2009, Paper PDPC2.
- [11] R. Dischler *et al.*, "Transmission of 3 \times 253-Gb/s OFDM-Superchannels over 764 km field deployed single mode fibers," presented at the Opt. Fiber Commun. Conf., San Diego, CA, 2010, Paper PDPA2.
- [12] S. Frisken, "Advances in liquid crystal on silicon wavelength selective switching," presented at the Opt. Fiber Commun. Conf., Anaheim, CA, 2007, Paper OWV4.
- [13] M. D. Feuer, D. C. Kilper, and S. L. Woodward, "ROADMs and their System Applications," in *Optical Fiber Telecommunications V-B*. New York: Academic, 2008.
- [14] T. A. Strasser and J. Taylor, "ROADMs unlock the edge of the network," *IEEE Commun. Mag.*, vol. 46, no. 7, pp. 146–149, Jul. 2008.
- [15] MM Research, Inc., Tucson, AZ.
- [16] D. J. F. Barros and J. M. Kahn, "Optimized dispersion compensation using orthogonal frequency-division multiplexing," *J. Lightw. Technol.*, vol. 26, no. 16, pp. 2889–2898, Aug. 2008.
- [17] J. G. Proakis, *Digital Communications*, 4th ed. New York: McGraw-Hill, 2002.
- [18] F. Sjoberg, M. Isaksson, R. Nilsson, S. K. Wilson, P. Odling, and P. O. Borjesson, "Zipper: A duplex method for VDSL based on DMT," *IEEE Trans. Commun.*, vol. 47, no. 8, pp. 1245–1252, Aug. 1999.
- [19] S. L. Jansen, I. Morita, T. C. W. Schenk, N. Takeda, and H. Tanaka, "Coherent optical 25.8-Gb/s OFDM transmission over 4160-km SSMF," *J. Lightw. Technol.*, vol. 26, no. 1, pp. 6–15, Jan. 2008.
- [20] T. M. Schmidl and D. C. Cox, "Robust frequency and timing synchronization for OFDM," *IEEE Trans. Commun.*, vol. 45, no. 12, pp. 1613–1621, Dec. 1997.
- [21] M. Sliskovic, "Carrier and sampling frequency offset estimation and correction in multicarrier systems," in *Proc. GLOBECOM*, 2001, pp. 285–289.
- [22] J. J. van de Beek, M. Sandell, and P. O. Borjesson, "ML estimation of time and frequency offset in OFDM systems," *IEEE Trans. Signal Process.*, vol. 45, no. 12, pp. 1800–1805, Jul. 1997.
- [23] S. Wu and Y. Bar-Ness, "OFDM systems in the presence of phase noise: Consequences and solutions," *IEEE Trans. Commun.*, vol. 52, no. 11, pp. 1988–1996, Nov. 2004.
- [24] K. P. Ho and J. M. Kahn, "Optical frequency comb generator using phase modulation in amplified circulating loop," *IEEE Photon. Technol. Lett.*, vol. 5, no. 6, pp. 721–725, Jun. 1993.
- [25] S. Bennett, B. Cai, E. Burr, O. Gough, and A. J. Seeds, "1.8-THz bandwidth, zero-frequency error, tunable optical comb generator for DWDM applications," *IEEE Photon. Technol. Lett.*, vol. 11, no. 5, pp. 551–553, May 1999.
- [26] Q. Zhuge, M. Morsy-Osman, and D. V. Plant, "Analysis of dispersion-enhanced phase noise in CO-OFDM systems with RF-pilot phase compensation," *Opt. Exp.*, vol. 19, no. 24, pp. 24030–24036, 2011.
- [27] X. Yi, W. Shieh, and Y. Ma, "Phase noise effects on high spectral efficiency coherent optical OFDM transmission," *J. Lightw. Technol.*, vol. 26, no. 10, pp. 1309–1316, May 2008.
- [28] M. Nazarathy *et al.*, "Phased-array cancellation of nonlinear FWM in coherent OFDM dispersive multi-span links," *Opt. Exp.*, vol. 16, no. 20, pp. 15777–15810, 2008.
- [29] Y. Tang, Y. Ma, and W. Shieh, "Performance impact of inline chromatic dispersion compensation for 107-Gb/s coherent optical OFDM," *IEEE Photon. Technol. Lett.*, vol. 21, no. 15, pp. 1042–1044, Aug. 2009.
- [30] M. Scholten, T. Coe, and J. Dillard, "Continuously-interleaved BCH (CI-BCH) FEC delivers best in class NECG for 40G and 100G metro applications," in *Proc. Opt. Fiber Commun. Conf.*, 2010, pp. 1–3.

Daniel J. F. Barros received the “*Licenciatura*” degree (Hons.) in electrical and electronics engineering from the University of Porto, Porto, Portugal, in 2004, and the M.S. and Ph.D. degrees in electrical engineering from Stanford University, Stanford, CA, in 2007 and 2011, respectively.

His research interests include optical fiber communications, wireless communications, digital signal processing, and RF circuits.

Joseph M. Kahn (M’90–SM’98–F’00) received the A.B., M.A., and Ph.D. degrees in physics from University of California Berkeley, Berkeley, in 1981, 1983, and 1986, respectively.

From 1987 to 1990, he was at AT&T Bell Laboratories, Crawford Hill Laboratory, Holmdel, NJ. He demonstrated multi-Gb/s coherent optical fiber transmission systems, setting world records for receiver sensitivity. From 1990 to 2003, he was on the Faculty of the Department of Electrical Engineering and Computer Sciences at University of California Berkeley, performing research on optical and wireless communications. Since 2003, he has been a Professor of electrical engineering at Stanford University, Stanford, CA, where he heads the Optical Communications Group. His current research interests include rate-adaptive and spectrally efficient modulation and coding methods, coherent detection and associated digital signal processing algorithms, digital compensation of fiber nonlinearity, high-speed transmission in multimode fiber, and free-space systems.

Dr. Kahn received the National Science Foundation Presidential Young Investigator Award in 1991. From 1993 to 2000, he served as a Technical Editor of IEEE PERSONAL COMMUNICATIONS MAGAZINE. Since 2009, he has been an Associate Editor of IEEE/OSA JOURNAL OF OPTICAL COMMUNICATIONS AND NETWORKING. In 2000, he helped found StrataLight Communications, where he served as Chief Scientist from 2000 to 2003. StrataLight was acquired by Opnext, Inc. in 2009.

Jeffrey P. Wilde (M’96) received the M.S. and Ph.D. degrees in applied physics from Stanford University, Stanford, CA, in 1989 and 1992, respectively. His thesis work involved the growth and characterization of photorefractive crystals for multiplex holography.

He has cofounded three companies having core technologies centered around optics and photonics. In 1994, he started 3-D Technology Labs to pursue materials development for holographic data storage. In 1996, he cofounded Quinta Corporation, a data-storage company based on a new type of high-capacity magneto-optic disk drive technology that utilized flying optical heads with single-mode fiber for light transmission and microelectromechanical systems mirrors for high-bandwidth track following. Quinta was acquired by Seagate Technology in 1997, and he subsequently served as the Director of Research West for Seagate. He left Seagate in 2000 and started Capella Photonics to develop wavelength switching technology for the optical telecommunications industry. Capella offers reconfigurable optical add-drop products for both metro and long-haul applications. Since 2003, he has served as a consultant and advisor for a range of companies. He is currently a Visiting Scholar with the Department of Electrical Engineering, Stanford University, Stanford, CA, where he is working on high-speed fiber communication technology.

Dr. Wilde is a member of the Optical Society of America.

Tarek Abou Zeid received the Diploma degree (Dipl.-Ing.) in electrical engineering from the University of Aachen RWTH, Aachen, Germany, in 2010.

In 2010, he joined Stanford University, Stanford, CA, as a Research Assistant within the Optical Communication Group. His research interests include single-mode optical fiber communications, nonlinear optics, and digital signal processing.